ISSN 1674-1056
http://cpb.iphy.ac.cn
http://iopscience.iop.org/cpb
中国物理 B
Chinese Physics
中国物理 Chinese Physics B

# High quantum efficiency long-/long-wave dual-color type-II InAs/GaSb infrared detector

Zhi Jiang(蒋志), Yao-Yao Sun(孙姚耀), Chun-Yan Guo(郭春妍), Yue-Xi Lv(吕粤希), Hong-Yue Hao(郝宏玥), Dong-Wei Jiang(蒋洞微), Guo-Wei Wang(王国伟), Ying-Qiang Xu(徐应强), Zhi-Chuan Niu(牛智川)

**Citation:**Chin. Phys. B . 2019, 28(3): 038504. **doi:** 10.1088/1674-1056/28/3/038504
Journal homepage: http://cpb.iphy.ac.cn; http://iopscience.iop.org/cpb

**What follows is a list of articles you may be interested in**

---

## Development of long-wavelength infrared detector and its space-based application requirements

Junku Liu(刘军库), Lin Xiao(肖林), Yang Liu(刘阳), Longfei Cao(曹龙飞), Zhengkun Shen(申正坤)
Chin. Phys. B . 2019, 28(2): 028504. **doi:** 10.1088/1674-1056/28/2/028504

## High material quality growth of AlInAsSb thin films on GaSb substrate by molecular beam epitaxy

Fa-Ran Chang(常发冉), Rui-Ting Hao(郝瑞亭), Tong-Tong Qi(齐通通), Qi-Chen Zhao(赵其琛), Xin-Xing Liu(刘欣星), Yong Li(李勇), Kang Gu(顾康), Jie Guo(郭杰), Guo-Wei Wang(王国伟), Ying-Qiang Xu(徐应强), Zhi-Chuan Niu(牛智川)
Chin. Phys. B . 2019, 28(2): 028503. **doi:** 10.1088/1674-1056/28/2/028503

## Recent advances in Ga-based solar-blind photodetectors

Ming-sheng Xu(徐明升), Lei Ge(葛磊), Ming-ming Han(韩明明), Jing Huang(黄静), Hua-yong Xu(徐化勇), Zai-xing Yang(杨再兴)
Chin. Phys. B . 2019, 28(2): 028502. **doi:** 10.1088/1674-1056/28/2/028502

## High quality $PdTe_2$ thin films grown by molecular beam epitaxy

En Li(李恩), Rui-Zi Zhang(张瑞梓), Hang Li(李航), Chen Liu(刘晨), Geng Li(李更), Jia-Ou Wang(王嘉鸥), Tian Qian(钱天), Hong Ding(丁洪), Yu-Yang Zhang(张余洋), Shi-Xuan Du(杜世萱), Xiao Lin(林晓), Hong-Jun Gao(高鸿钧)
Chin. Phys. B . 2018, 27(8): 086804. **doi:** 10.1088/1674-1056/27/8/086804

## Comparison of blue-green response between transmission-mode GaAsP-and GaAs-based photocathodes grown by molecular beam epitaxy

Gang-Cheng Jiao(焦岗成), Zheng-Tang Liu(刘正堂), Hui Guo(郭晖), Yi-Jun Zhang(张益军)
Chin. Phys. B . 2016, 25(4): 048505. **doi:** 10.1088/1674-1056/25/4/048505

---

# High quantum efficiency long-/long-wave dual-color type-II InAs/GaSb infrared detector*

Zhi Jiang(蒋志)[1,2], Yao-Yao Sun(孙姚耀)[1,2], Chun-Yan Guo(郭春妍)[1,2], Yue-Xi Lv(吕粤希)[1,2], Hong-Yue Hao(郝宏玥)[1,2], Dong-Wei Jiang(蒋洞微)[1,2], Guo-Wei Wang(王国伟)[1,2,‡], Ying-Qiang Xu(徐应强)[1,2], and Zhi-Chuan Niu(牛智川)[1,2,†]

[1] *State Key Laboratory for Superlattices and Microstructures, Institute of Semiconductors, Chinese Academy of Sciences, Beijing* 100083, *China*
[2] *Center of Materials Science and Optoelectronics Engineering, University of Chinese Academy of Sciences, Beijing* 100049, *China*

(Received 14 December 2018; revised manuscript received 14 January 2019; published online 26 February 2019)

A long-/long-wave dual-color detector with N-M-$\pi$-B-$\pi$-M-N structure was developed based on a type-II InAs/GaSb superlattice. The saturated responsivity was achieved under low bias voltage for both channels. The device could be operated as a single detector for sequential detection and showed high quantum efficiencies. The peak quantum efficiencies of long-wavelength infrared band-1 (blue channel) and long-wavelength infrared band-2 (red channel) were 44% at 6.3 μm under 20 mV and 57% at 9.1 μm under −60 mV, respectively. The optical performance for each channel was achieved using a 2 μm thickness absorber. Due to the high QE, the specific detectivities of the blue and red channels reached $5.0\times10^{11}$ cm·Hz$^{1/2}$/W at 6.8 μm and $3.1\times10^{11}$ cm·Hz$^{1/2}$/W at 9.1 μm, respectively, at 77 K.

**Keywords:** infrared detector, InAs/GaSb superlattice, dual-color, molecular beam epitaxy

**PACS:** 85.60.Gz, 68.65.Cd, 72.20.Jv **DOI:** 10.1088/1674-1056/28/3/038504

## 1. Introduction

Type-II InAs/GaSb superlattices (T2SLs), first proposed by Sai-Halasz *et al.* in the 1970s,[1] offer an alternative means of infrared detection and imaging. Mercury-cadmium telluride (MCT) photodetectors have several issues: they are toxic, relatively costly, and can be inhomogeneous over large wafers. Long-wavelength infrared (LWIR) MCT photodetectors are often limited by Auger recombination, which T2SLs have been theorized to be able to suppress, which could potentially lead to better performance. Furthermore, T2SLs have already demonstrated high external quantum efficiencies (QEs) of up to 50% in the LWIR.[2] Infrared detectors with P$\pi$MN-structure[3,4] and unipolar barrier structure[5,6] have been developed. In those studies, T2SLs have shown flexibility in device structure design to improve the detector performance.[7–9] Multi-color/band detectors can contribute to enhancing image contrast or target recognition.[8–10] Detectors configured for LWIR/LWIR detection are used for clutter rejection in a wide variety of space and ground-based applications.[11,12]

In this work, a long-/long-wave dual-color detector with high QE based on an N-M-$\pi$-B-$\pi$-M-N structure was first developed. The blue and red channels with 50% cutoff wavelengths at 7.6 μm and 11.5 μm, respectively, presented QEs of 44% and 57% at 77 K. In the structure, the M-structure barrier was used to suppress the dark current. And in order to inhibit cross-talk, an $Al_{0.2}Ga_{0.8}Sb$ layer was sandwiched between the blue and the red channels.

## 2. Experiment

### 2.1. Material and structure

The band structure of the M-structure superlattice is shown in Fig. 1(a). Its periodic structure was composed of 18 monolayers (MLs) InAs/3 MLs GaSb/5 MLs AlSb/3 MLs GaSb. The thin AlSb layer in the M-structure affects both electrons in the conduction band and holes in the valence band. It forms a more effective barrier that blocks the tunneling of the electrons in the two adjacent InAs wells. For holes, the AlSb layer causes the GaSb layer to become a double quantum well, which elevates the first and the second valence bands. Therefore, with the high electron effective mass in the M-structure, the transport of electrons in the depletion region due to diffusion and tunneling would have more resistance, and the dark current is expected to decrease.[3] Our device was grown using a molecular beam epitaxy (MBE) system (Veeco Epi Gen II) based on an N-type GaSb (100) substrate. The substrate was double-side polished to avoid strain relaxation and interface related defects.[13] The structure and band diagram of the device are shown in Fig. 1(b). First, an N-type GaSb buffer with thickness of 900 nm was grown between the substrate and the red channel contact region, which ensures an atomically smooth surface for the device growth. Then, the 2 μm thick lightly Be-doped ($p \approx 4$–$6\times10^{16}$ cm$^{-3}$) active region superlattice for the red channel was grown with 14 MLs of InAs and 7 MLs of GaSb per period, while the blue channel grown subsequently had an 11 MLs InAs/7 MLs GaSb design with the same total thickness. Both Si-doped

*Project supported by the National Key Technology R&D Program of China (Grant Nos. 2018YFA0209104 and 2016YFB0402403).
†Corresponding author. E-mail: zcniu@semi.ac.cn
‡Corresponding author. E-mail: wangguowei@semi.ac.cn
© 2019 Chinese Physical Society and IOP Publishing Ltd 

N regions ($n \approx 1 \times 10^{18}$ cm$^{-3}$) were composed of a 0.5 μm thick M-superlattice. The M-structure barrier regions with thickness of 0.5 μm were undoped. A 0.2 μm Be-doped ($p \approx 8 \times 10^{16}$ cm$^{-3}$) $Al_{0.2}Ga_{0.8}Sb$ barrier was sandwiched between the two channels. Finally, the entire structure was capped off with a 0.02 μm thick N-type ($n \approx 2 \times 10^{18}$ cm$^{-3}$) InAs layer.

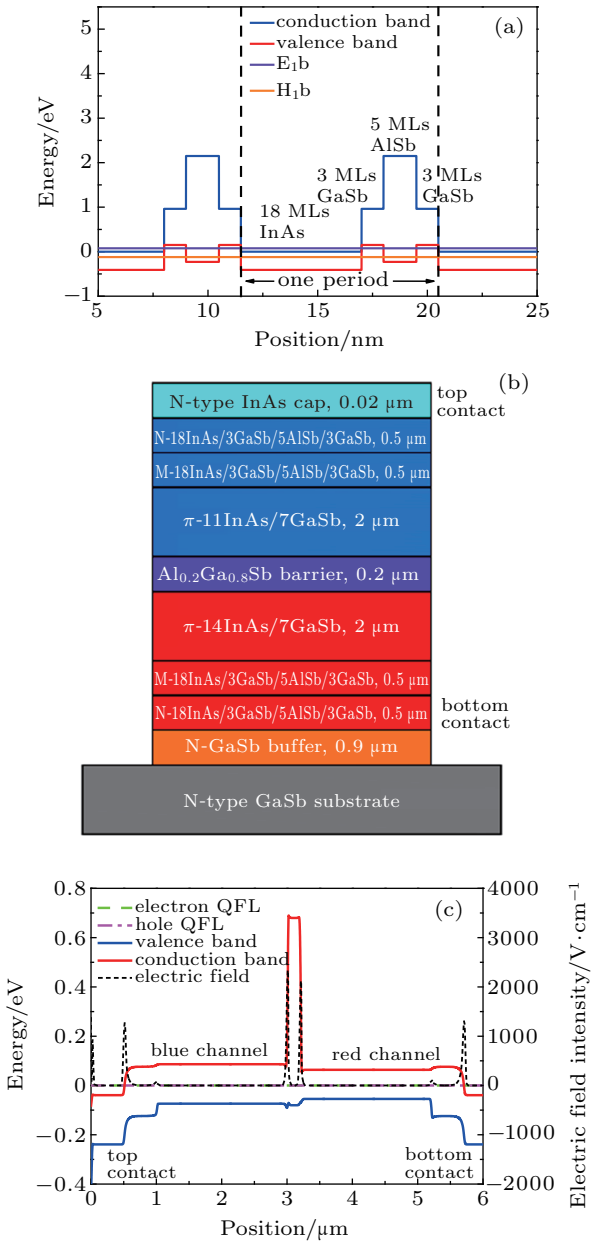



**Fig. 1.** (a) The band diagram of the M-structure, where $E_1b$ and $H_1b$ represent the band edges of the first electron energy levels and the first hole energy levels in the minibands, respectively. (b) The structure diagram and (c) band alignment of the LW/LW dual-color detector, where the electron QFL and hole QFL represent quasi Fermi levels.

The band alignment and distribution of electrical field intensity are shown in Fig. 1(b). The valence band offset between the red and blue channels was almost eliminated. This means that the device could be operated under low bias voltage. The electrical field drop is small across both absorber regions, since there is a significant amount of field drop across the wider-bandgap barrier layers. This reduction in electric field will lead to small depletion regions and hence a reduction in the generation–recombination current ($J_{gr}$) and tunneling current.

The mismatch of each superlattice was measured using symmetric (004) x-ray diffraction. The high-resolution x-ray diffraction (HRXRD) pattern is shown in Fig. 2(a). Table 1 lists the parameters of each superlattice in the device. All of the contained superlattices' periodic thicknesses match well with our design. The full width at half maximum (FWHM) shows the high crystalline quality of the epi-layers. The morphology of the sample was characterized by differential interference microscopy (Nikon ECLIPSE) (Fig. 2(b)) and atomic force microscopy (AFM) (Fig. 2(c)). In an area of 870 μm×650 μm, the epi-layer exhibits flatness and non-defective morphology. The AFM scanning result shows the atomic step edge. And the root-mean-square (RMS) of roughness is 1.9 Å over a 10 μm×10 μm area.

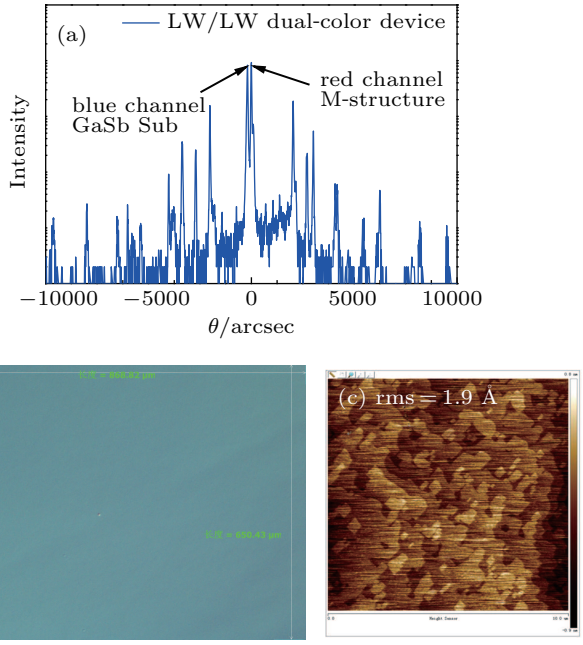



**Fig. 2.** (a) HRXRD pattern, (b) differential interference micrograph, and (c) AFM image of the device.

**Table 1.** The mismatch, period, and FWHM of 0$^{th}$ peaks of different superlattices.

| Superlattice | Blue channel | Red channel | M-structure |
|---|---|---|---|
| Mismatch/(″) | 14 | 191 | 191 |
| Theoretical period/Å | 58 | 68 | 92 |
| Actual period/Å | 58 | 68 | 91 |
| FWHM/arcsec | 36 | 39.6 | 39.6 |

## 2.2. Device fabrication

The mesas with different sizes (200 μm, 300 μm, 500 μm) were defined through lithography (SUSS MA6) and fabricated by dry etching through the InAs cap layer (top contact) and each region into the red channel N-type contact (bot-

tom contact). The $SiO_2$ hard etching mask (PECVD STS) and inductively coupled plasma (ICP OXFORD plasmalab System 100) system were chosen to etch the mesa. The sidewall was passivated using anodic sulfide, then covered by a 200 nm $SiO_2$ layer. The $SiO_2$ layer was deposited using ion beam sputtering (OXFORD optofab3000). After the above steps, a second photolithography and ICP were performed to open the window on the passivation layer. The final metal electrode was deposited using electron beam evaporation (SKY EB700-I).

## 3. Results and discussion

### 3.1. Spectral response

The working mechanism is similar to that of the dual-band detector which was mentioned in Ref. [14]. The optical characterization of the front-side illuminated detector was performed at 77 K using a Fourier transform infrared (FTIR) spectrometer (Bruker Vertex70) and a calibrated black-body (SYSTEMS) source at a temperature of 500 °C. The FTIR spectrometer was calibrated by using a standard DTGS detector without anti-reflection (AR) coating. Figure 3 shows the optical performance of the detector with diameter 300 μm. It is defined as forward bias when the applied bias on the top contact is positive with respect to the bottom contact. Otherwise, it is defined as reverse bias. The blue channel exhibits a peak responsivity ($R_i$) of 2.4 A/W at 6.8 μm under 20 mV, while the red channel shows a peak $R_i$ of 4.2 A/W at 9.1 μm under a bias of −60 mV. The 50% QE cutoff wavelengths are measured at 7.6 μm and 11.5 μm. The peak QEs of the blue and red channels are 44% at 6.3 μm and 57% at 9.1 μm, respectively. From Fig. 3(c), the bias range above −20 mV corresponds to the transport of minority electrons in the blue channel, while the bias range below −20 mV corresponds to the transport of minority electrons in the red channel. The applied bias is small enough to be suitable for focal plane arrays (FPAs) operation. In order to quantify the optical cross-talk, we use a selectivity parameter ($S$) defined as follows:[15]

$$S_{\text{blue}} = \frac{QE^{\text{blue}}_{9.1\ \mu\text{m}}}{QE^{\text{blue}}_{6.3\ \mu\text{m}}}, \tag{1}$$

$$S_{\text{red}} = \frac{QE^{\text{red}}_{6.3\ \mu\text{m}}}{QE^{\text{red}}_{9.1\ \mu\text{m}}}, \tag{2}$$

where $QE^{\text{blue}}_{9.1\ \mu\text{m}}$, $QE^{\text{blue}}_{6.3\ \mu\text{m}}$, $QE^{\text{red}}_{9.1\ \mu\text{m}}$, and $QE^{\text{red}}_{6.3\ \mu\text{m}}$ are the QEs of the blue and red channels at 9.1 μm and 6.3 μm, respectively. Using these parameters, the selectivities of the blue and red channels are 0.46 and 0.02, respectively. The low $S_{\text{blue}}$ demonstrates that the photoexcited electrons in the red channel are blocked by the $Al_{0.2}Ga_{0.8}Sb$ barrier. The $S_{\text{red}}$ is poor because the 2 μm thick absorber of the blue channel means it is hard to fully suppress the response of the red channel below 8 μm. Under a bias of −50 mV, the detector shows the lowest $S_{\text{red}}$ of 0.21. Assuming there is no internal reflection inside the device, we can estimate how much IR signal is stopped by the blue channel. The blue channel blocks 60% of the IR radiation between 3 μm and 8 μm. The optical cross-talk can be effectively suppressed by increasing the absorber thickness. Table 2 lists the published results and our result; the performance of our single-unit device approaches, or even surpasses, that of the previous ones.

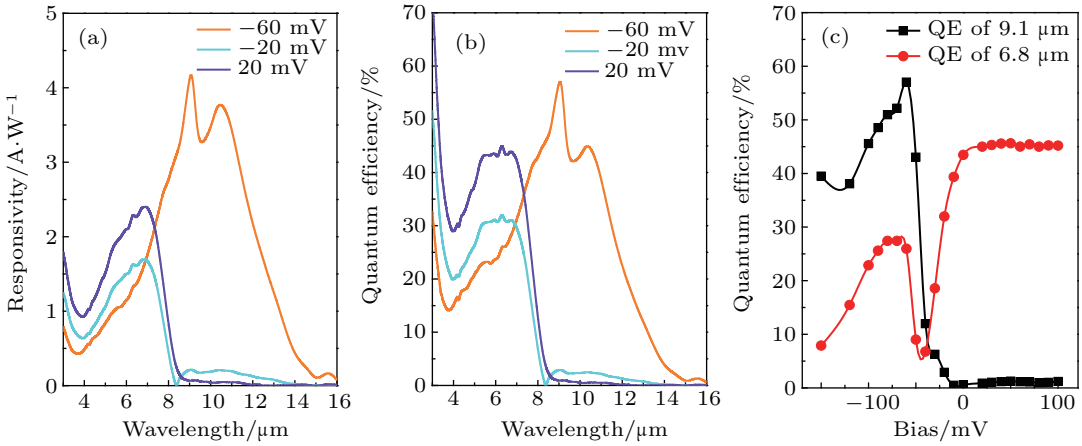



**Fig. 3.** (a) Spectral responsivity and (b) quantum efficiency under −60 mV, −20 mV, and 20 mV at 77 K. (c) The variation of quantum efficiency with applied bias for wavelengths of 9.1 μm and 6.3 μm at 77 K.

**Table 2.** Comparison with published results.

| | Structure | Red channel peak QE/% | Applied bias/mV | Blue channel peak QE/% | Applied bias/mV |
|---|---|---|---|---|---|
| Ref. [11] | N-M-π-P-P-P-π-M-N | 45@6.3 μm | –50 | 43@10.2 μm | 150 |
| Ref. [12] | pBp | 38@6.5 μm | 90 | 34@9.81 μm | –100 |
| This work | N-M-π-B-π-M-N | 44@6.3 μm | 20 | 57@9.1 μm | –60 |

### 3.2. The *I–V* characterization

The dark current density ($J$) was measured using Agilent B1500 in the bias range from 0.3 V to −0.3 V at 77 K. As shown in Fig. 4(a), the blue and red channels of the device with diameter 300 μm show dark currents of $8.5\times10^{-5}$ A/cm$^2$ at 20 mV and $4.6\times10^{-4}$ A/cm$^2$ at −60 mV, respectively. The differential resistance and area products $RA$ are 201 Ω·cm$^2$ under 20 mV and 67 Ω·cm$^2$ under −60 mV at 77 K. The linear fitting of inverse $RA$ vs. $P/A$ is shown as a function of $P/A$ for the devices with diameter 500 μm, 300 μm, and 200 μm in Fig. 4(b), and the bulk-limited resistances of the blue and red channels are 1000 Ω·cm$^2$ and 179 Ω·cm$^2$, respectively. The surface resistivity is equal to $2.9\times10^4$ Ω·cm and $9.1\times10^3$ Ω·cm for the blue and red channels, respectively, at 77 K. For both channels, the relatively high surface resistivity shows suppressed surface related currents, but the bulk-limited resistance is not large enough to block the bulk leakage.[12] As a result, the main dark current comes from bulk leakage. Compared with the results published in Refs. [11] and [12], the dark current density of our blue channel is relatively high. The bulk leakage was fitted by referencing the published result.[16] As shown in Fig. 4(c), the main leakage in both channels under operating bias is $J_{gr}$. The M-structure barrier in the blue channel fails to take most part of the applied bias. Therefore, a large part of the p-side depletion region lies within the absorber layer, giving rise to large $J_{gr}$. A narrow width of the depletion region in the absorber is beneficial for decreasing $J_{gr}$. It may be useful to decrease the depletion region width in the blue channel by using the periodic structure of 18 MLs InAs/5 MLs GaSb/5 MLs AlSb/5 MLs GaSb to replace the currently used M-structure. And the high density of recombination centers in the absorber also results in large $J_{gr}$. Another main dark current source is the trap-assisted tunneling current ($J_{TAT}$) that depends on the trap density and the effective mass of the electrons. And in theory, the recombination centers and trap states can be eliminated by optimizing the superlattices' growth conditions.

Figure 5(a) collects dark current densities of the blue and red channels for comparison with "Rule 07". The cutoff wavelength is taken as the point of a 50% response. The experimental data of the blue channel show considerably greater leakage current than Rule 07 by some orders of magnitude, while the current density of the red channel is close to Rule 07. The trend is that it is generally more difficult to control dark current at the shorter wavelength.[17] The specific detectivity ($D^*$) spectrum is shown in Fig. 5(b).

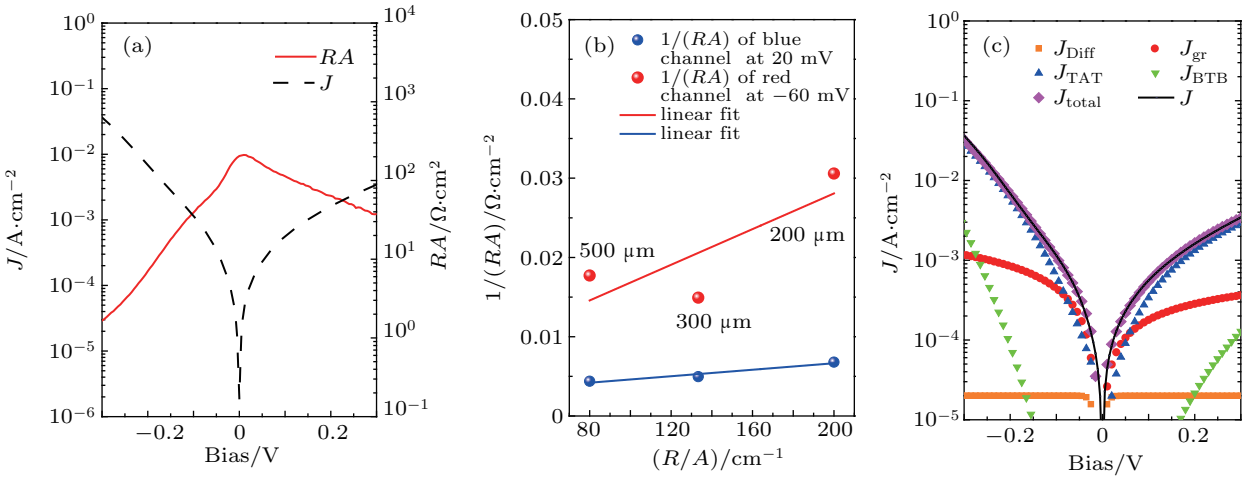



**Fig. 4.** (a) Dark current density $J$, differential resistance and area products $RA$ of the dual-color detector with mesa diameter 300 μm. (b) The inverse $RA$ vs. $P/A$ is shown as a function of $P/A$ for the detectors with different sizes. (c) Measured and modeled dark current of the LW/LW dual-color detector under bias from −0.3 V to 0.3 V.

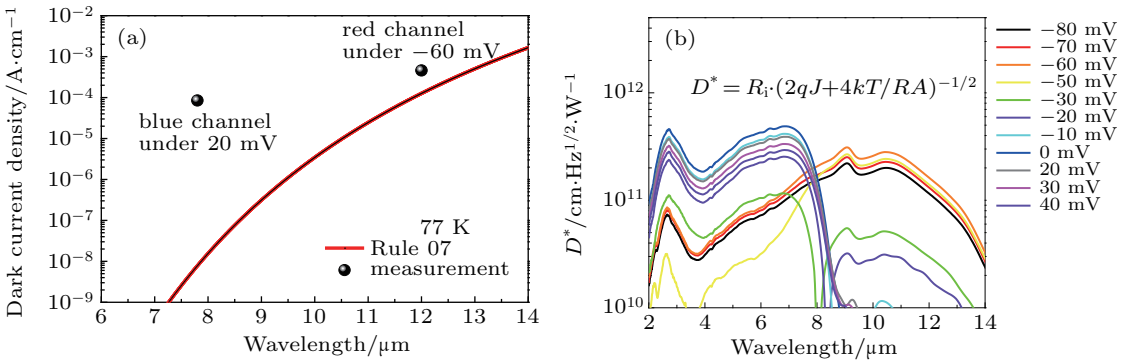



**Fig. 5.** (a) The 77 K dark current densities plotted against cutoff wavelength for the blue channel under 20 mV and the red channel under −60 mV. The solid line indicates the dark current density calculated using the empirical Rule 07 model. (b) The specific detectivity spectrum of both channels at different applied bias voltages.

At 77 K, the maximum $D^*$ for the blue channel is $5.0 \times 10^{11}$ cm·Hz$^{1/2}$/W at 6.8 μm under 0 mV, while the red channel has $3.1 \times 10^{11}$ cm·Hz$^{1/2}$/W at 9.1 μm under −60 mV. The specific detectivity can be enhanced by increasing the absorber thickness and inhibiting dark current density.

## 4. Conclusion and perspectives

In this work, a long-/long-wave dual-color detector based on an InAs/GaSb superlattice with N-M-$\pi$-B-$\pi$-M-N structure was successfully fabricated and characterized. The peak QEs of the blue and red channels are 44% at 6.3 μm under 20 mV and 57% at 9.1 μm under −60 mV, respectively. And the corresponding responsivities of the blue and red channels are 2.4 A/W at 6.8 μm and 4.2 A/W at 9.1 μm, respectively. The optical performance was measured based on a 2 μm thick absorber. The maximum $D^*$ for the blue channel is $5.0 \times 10^{11}$ cm·Hz$^{1/2}$/W at 6.8 μm without applied bias, while it is $3.1 \times 10^{11}$ cm·Hz$^{1/2}$/W at 9.1 μm under −60 mV for the red channel. In order to achieve better performance, the device structure and fabrication process of the dual-color detector both need to be further optimized.

## References


[1] Sai-Halasz G A, Tsu R and Esaki L 1977 *Appl. Phys. Lett.* **30** 651

[2] Nguyen B M, Hoffman D, Wei Y J, Delaunay P Y, Hood A and Razeghi M 2007 *Appl. Phys. Lett.* **90** 231108

[3] Nguyen B M, Hoffman D, Delaunay P Y and Razeghi M 2007 *Appl. Phys. Lett.* **91** 163511

[4] Huang E K, Pour S A, Hoang M A, Haddadi A, Razeghi M and Tidrow M Z 2012 *Opt. Lett.* **37** 2025

[5] Ting D Z, Hill C J, Soibel A, Keo S A, Mumolo J M, Nguyen J and Gunapala S D 2009 *Appl. Phys. Lett.* **95** 023508

[6] Rodriguez J B, Plis E, Bishop G, Sharma Y D, Kim H, Dawson L R and Krishna S 2007 *Appl. Phys. Lett.* **91** 043514

[7] Han X, Xiang W, Hao H Y, Jiang D W, Yao Y, Wang G W, Xu Y Q and Niu Z C 2017 *Chin. Phys. B* **26** 018505

[8] Jiang Z, Han X, Sun Y Y, Guo C Y, Lv Y X, Hao H Y, Jiang D W, Wang G W, Xu Y Q and Niu Z C 2017 *Infrared Phys. Technol.* **86** 159

[9] Jiang D W, Xiang W, Guo F Y, Hao H Y, Han X, Li X C, Wang G W, Xu Y Q, Yu Q J and Niu Z C 2016 *Chin. Phys. Lett.* **33** 048502

[10] Sun Y Y, Lv Y X, Han X, Guo C Y, Jiang Z, Hao H Y, Jiang D W, Wang G W, Xu Y Q and Niu Z C 2017 *Chin. Phys. B* **26** 098506

[11] Huang E K and Razeghi M 2012 *SPIE Proceedings - The International Society for Optical Engineering*, 21–26 January 2012, San Francisco, United States, 82680Z

[12] Plis E, Myers S A, Ramirez D A and Krishna S 2016 *SPIE Defense + Security*, 17–21 April 2016, Baltimore, United States, 981911

[13] Rodriguez J B, Christol P, Cerutti L, Chevrier F and Joullié A 2005 *J. Cryst. Growth* **274** 6

[14] Ariyawansa G, Grupen M, Duran J M, Scheihing J E, Nelson T R and Eismann M T 2012 *J. Appl. Phys.* **111** 073107

[15] Razeghi M, Haddadi A, Dehzangi A, Chevallier R and Yang T 2017 *SPIE Defense + Security*, 9–13 April 2017, Anaheim, United States, 1017705

[16] Martyniuk P, Wrobel J, Plis E, Madejczyk P, Kowalewski A, Gawron W, Krishna S and Rogalski A 2012 *Semicond. Sci. Technol.* **27** 055002

[17] Rogalski A, Martyniuk P and Kopytko M 2017 *Appl. Phys. Rev.* **4** 031304